2008

Spectral Tomography with Diffuse Near-Infrared Light: Inclusion of Broadband Frequency Domain Spectral Data

Jia Wang

Scott C. Davis

Subhadra Srinivasan

Shudong Jiang

Published in final edited form as:
J Biomed Opt. 2008 ; 13(4): 041305. doi:10.1117/1.2952006.

Spectral tomography with diffuse near-infrared light: inclusion of broadband frequency domain spectral data

Jia Wang,
Dartmouth College, Department of Physics and Astronomy, Hanover, New Hampshire

Scott C. Davis,
Dartmouth College, Thayer School of Engineering, Hanover, New Hampshire

Subhadra Srinivasan,
Dartmouth College, Thayer School of Engineering, Hanover, New Hampshire

Shudong Jiang,
Dartmouth College, Thayer School of Engineering, Hanover, New Hampshire

Brian W. Pogue, and
Dartmouth College, Thayer School of Engineering, Hanover, New Hampshire

Keith D. Paulsen
Dartmouth College, Thayer School of Engineering, Hanover, New Hampshire

Abstract

Near-infrared (NIR) region-based spectroscopy is examined for accuracy with spectral recovery using frequency domain data at a discrete number of wavelengths, as compared to that with broadband continuous wave data. Data with more wavelengths in the frequency domain always produce superior quantitative spectroscopy results with reduced noise and error in the chromophore concentrations. Performance of the algorithm in the situation of doing region-guided spectroscopy within the MRI is also considered, and the issue of false positive prior regions being identified is examined to see the effect of added wavelengths. The results indicate that broadband frequency domain data are required for maximal accuracy. A broadband frequency domain experimental system was used to validate the predictions, using a mode-locked Ti:sapphire laser for the source between 690- and 850-nm wavelengths. The 80-MHz pulsed signal is heterodyned with photomultiplier tube detection, to lower frequency for data acquisition. Tissue-phantom experiments with known hemoglobin absorption and tissue-like scatter values are used to validate the system, using measurements every 10 nm. More wavelengths clearly provide superior quantification of total hemoglobin values. The system and algorithms developed here should provide an optimal way to quantify regions with the goal of image-guided breast tissue spectroscopy within the MRI.

Keywords

frequency domain; region-guided spectroscopy; spectral tomography; near infrared

Address all correspondence to: Brian W. Pogue, Thayer School of Engineering, Dartmouth College, 8000 Cummings Hall, Hanover, New Hampshire, 03755; Tel: +603–646–3861; Fax: +603–646–3856; pogue@dartmouth.edu.

1 Introduction

Near-Infrared (NIR) tomography systems have recently been developed that transition the modality away from stand-alone imaging systems toward hybrid-modality combinations with standard clinical imaging systems. To optimize this approach with respect to optical tomography, some important hardware and software specifications need to be determined. In this study, the theoretical and experimental foundations for incorporating broadband NIR tomography into MRI breast imaging have been examined. Issues related to the choices of NIR spectroscopy hardware have been evaluated, including the impact of frequency-domain versus continuous-wave data, as well as the extent to which the wavelength band used in the measurements affects the accuracy. The goal of the work has been to investigate the optimal way of achieving quantitative spectroscopy of MRI-directed tissue regions, through theoretical and basic experimental analysis of different measurement systems.

In magnetic resonance imaging (MRI) of the breast, multiple abnormalities are commonly observed because women are referred to MRI when there is complex tissue architecture.[1] As a result, the number of false positive abnormalities can be quite high, and augmenting this detection with additional diagnostic information would be a way to increase specificity. Quantitative NIR spectroscopy could be applied to MRI-defined tissue regions as a means of providing molecular-specific information. Applying existing NIR tomography methods to MR breast imaging has been demonstrated in previous work.[2–4]

Integrating MRI-derived structural information into NIR image reconstruction was initially considered theoretically by Barbour et al.,[5] Arridge and Schwelger,[6] and Pogue and Paulsen.[7] These studies applied simple segmentation methods to define homogenous tissue volumes. The approach was used experimentally by Ntziachristos et al.[8] to quantify optical indocyanine green in breast cancers whose shape was identified by MRI. Assigning tissue volumes to be homogenous regions optically produces a hard encoding of the prior information, which reduces the number of unknown estimation parameters and results in a sufficiently well-conditioned NIR reconstruction problem to not require regularization. Alternatively, the spatial priors can be encoded through a regularization matrix, as demonstrated by Brooksby et al.[4,9] and Carpenter et al.[3] This strategy produces soft encoding of the MRI structure,[10] which still allows tissue heterogeneity to exist within the pre-defined regions. The critical challenge for NIR is to provide information that reduces the false positive identification of breast abnormalities by quantifying suspicious volumes definable from MRI. Implementation of NIR spectroscopy on MRI breast volumes was investigated in this study, with the goal of determining which approach more accurately quantifies abnormalities embedded within the fibroglandular tissue of the breast.

NIR spectroscopy of breast has been able to quantify both normal and tumor tissues based on differences in chromophore concentrations and scattering properties.[11–19] Studies have shown that tumors are detectable from normal tissue based on local increases in blood and water, or through injection of optical contrast agents such as indocyanine green. But quantification of these regions requires multiple wavelengths[20] and direct measurements of scattering path length[21,22] to attain an acceptable degree of accuracy in the recovered values. While these factors have been studied extensively without prior information, it is not clear how much spectral data are required in the setting of MRI guided priors. In particular, spectral bandwidth is a critical design specification in the development of a spectroscopic tomography system. Generally, the use of more wavelengths leads to higher quantitative accuracy; yet, it also increases the data acquisition time and computational complexity. Ideally, the minimum number of optical wavelengths would be used to quantify regions defined by MRI. Additionally, the importance of a phase shift measurement in differentiating absorption from scattering has been recognized for many years[23–26];

however, this requires the use of photomultiplier tubes that have fast temporal response, yet suffer from a loss of response beyond a wavelength of 850 nm. It is possible that including more continuous wave wavelengths when combined with spectrally constrained reconstruction could compensate for not incorporating the phase data from the narrower band frequency domain (FD) detection. The tradeoff between number of wavelengths and image accuracy was studied here using actual breast parenchymal patterns and experimental phantom data representing tissue. The use of continuous wave (cw) versus amplitude-modulated (FD) light to perform the spectroscopy was also examined. Thus, it is important to recognize that the choice of measurement type (cw versus FD) also impacts the wavelength range that can be used, because of the photocathode efficiency change of the two detectors with maximal detection efficiency (solid-state devices for cw versus photomultiplier tubes for FD).

In addition to simulations, multiwavelength phantom results acquired with a new frequency domain system using a Ti: sapphire laser demonstrated the advantage of adding more spectral constraints in the inverse problem. The system developed in this study is a unique design, allowing a continuum of FD measurements across the NIR, within the detection range of the photomultiplier tube detection. The use of many wavelengths of FD data collection is demonstrated for the first time, and the optimal path for development of a finished clinical system is discussed.

Design choices for MRI-guided diffuse spectroscopy for breast imaging will benefit from the results of this theoretical analysis. Breast MRI images were used as the background to test multispectral chromophore reconstruction. The primary metric used in the analysis was the accuracy in the recovered chromophore concentrations within local regions of fibroglandular tissue defined by MRI images.

2 Materials and Methods

2.1 Theory

The propagation of NIR light in tissue is modeled with the radiative transfer equation based on the approximation that scattering dominates absorption over large distances in breast tissue,[27] in which case

$$-\nabla \bullet D(r)\nabla\Phi(r,\omega)+\left[\mu_a(r)+\frac{i\omega}{c}\right]\Phi(r,\omega)=q_0(r,\omega),$$

where $q_0(r,\omega)$ is an isotropic light source at position r, $\Phi(r,\omega)$ is the isotropic fluence at modulation frequency ω, and c is the speed of light in tissue. The two image reconstruction parameters in the transfer equation are the absorption coefficient $\mu_a(r)$ and diffusion coefficient $D(r)$. Here, $D(r)$ can be written as

$$D(r)=\frac{1}{3[\mu_a(r)+\mu_s'(r)]},$$

where the reduced scattering coefficient $\mu_s'(r)=\mu_s(r)[1-g(r)]$, $\mu_s(r)$ is the scattering coefficient, and the anisotropy factor $g(r)$ is the mean cosine of the single scatter function. The measurement data at the tissue surface Φ includes two parts: the amplitude and phase shift of transmitted light at frequency ω. The absorption and scattering process in the tissue determine both amplitude and phase. Amplitude is considered as measurement of

attenuation of light, while phase mainly represents the optical path length of transmitted light. The complete set of boundary data can provide information about the spatial distribution of the absorption and reduced scattering coefficients. Solving for the distribution of optical properties is a nonlinear inverse problem. A finite-element-based reconstruction algorithm is used and the solution is obtained with a Newton-minimization method.[25] The optical parameters are updated iteratively by the equation:

$$\delta\mu=(\boldsymbol{J}^T\boldsymbol{J}+\lambda I)^{-1}\boldsymbol{J}^T[\Phi_m-\Phi_c],$$

where Φ_m is the measurement data and Φ_c is the modeled data; $\boldsymbol{J}$ is the Jacobian matrix that describes the sensitivity of the measurement data to the optical properties. $\boldsymbol{J}^T\boldsymbol{J}$ is an ill-conditioned matrix, so regularization λ is added to the diagonal terms. The iteration continues to update the optical property parameters until the change in projection error is less than 2% between successive iterations.

This method of reconstruction processes the measurement data from each wavelength independently to calculate μ_a and μ_s'.[28] The concentrations of chromophores are estimated with μ_a based on Beer's law, which indicates that the total absorption coefficient is a linear combination of the individual chromophore contributions to absorption;

$$\mu_a(\lambda)=\sum_{i=1}^{N}\varepsilon_i(\lambda)C_i,$$

where N is the total number of chromophores in the tissue, C_i is the concentration of each chromophore, and $\xi_i(\lambda)$ is the molar absorption coefficient of each chromophore indexed by i. Three chromophore components are assumed here: oxyhemoglobin (HbO_2), deoxyhemoglobin (Hb), and water. Scattering properties (scattering amplitude a and scattering power b) are found by constructing a best fit to an empirical approximation to the Mie scattering theory.[29,30]

$$\mu_s'(\lambda)=a\lambda^{-b}.$$

It has been shown that the reconstruction can be significantly improved if spectral constraints are directly imposed in the reconstruction, because datasets from multiple wavelengths are used simultaneously.[20] The key step in direct spectral reconstruction is mapping the Jacobian matrix from optical property parameter space (μ_a and μ_s') to chromophore concentration and scattering parameter space:

$$\boldsymbol{J}_c=\boldsymbol{J}_{\mu_a}\times\frac{\partial\mu_a}{\partial c},\quad \boldsymbol{J}_a=\boldsymbol{J}_D\times\frac{\partial D}{\partial a},\quad \boldsymbol{J}_b=\boldsymbol{J}_D\times\frac{\partial D}{\partial b},$$

where the number of unknowns is scaled by the number of chromophores plus the number of scattering parameters. With direct spectral reconstruction, data from multiple wavelengths can be processed simultaneously due to the wavelength independence of the chromophore concentration and scattering parameters.[20] In this work, simulations with different numbers of wavelengths were compared to explore the effect of implementing broadband spectral constraints.

Although spectral reconstruction estimates wavelength-independent parameters, the number of unknowns is still much larger than the number of measurements. Therefore, incorporating prior structural (anatomical) information is important during image reconstruction to decrease the illposedness of the inverse problem.[31] Knowledge of tissue structure from MRI includes the parenchymal pattern of adipose and fibroglandular tissue along with the position of possible tumor targets.

Two kinds of methods can be used to incorporate prior structure into an iterative reconstruction process: soft priors[9] and hard priors.[31,32] The hard-priors approach segments the image space into several regions based on MRI, where each region is also assumed to be optically homogenous. Thus, iterative updating is simplified to estimating the parameters associated with a small number of homogenous regions that comprise the heterogeneous image. In the process of reconstruction, the Jacobian matrix is multiplied by a spatial prior matrix $\boldsymbol{K}$, given by,

$$\boldsymbol{K}=\begin{bmatrix} k_{1,1}^{c1} & k_{1,2}^{c1} & \cdots & k_{1,NR}^{c1} \\ k_{2,1}^{c1} & k_{2,2}^{c1} & \cdots & k_{2,NR}^{c1} \\ \vdots & \vdots & \ddots & \vdots \\ k_{NN,1}^{c1} & k_{NN,2}^{c1} & \cdots & k_{NN,NR}^{c1} \\ k_{1,1}^{c2} & k_{1,2}^{c2} & \cdots & k_{1,NR}^{c2} \\ k_{2,1}^{c2} & k_{2,2}^{c2} & \cdots & k_{2,NR}^{c2} \\ \vdots & \vdots & \ddots & \vdots \\ k_{NN,1}^{c2} & k_{NN,2}^{c2} & \cdots & k_{NN,NR}^{c2} \\ k_{1,1}^{c3} & k_{1,2}^{c3} & \cdots & k_{1,NR}^{c3} \\ k_{2,1}^{c2} & k_{2,2}^{c2} & \cdots & k_{2,NR}^{c2} \\ \vdots & \vdots & \ddots & \vdots \end{bmatrix},$$

here, $k_{i,j}=1$ if node i and j are in the same region, or $k_{i,j}=0$ if nodes i and j are not in the same region. NR is the number of regions produced by the structural segmentation, NN is the number of nodes, and c_i is the chromophore or scattering parameter. A new Jacobian matrix is constructed, where all of the columns of the same regions are summed. The number of unknown parameters is significantly decreased, because only those associated with the individual regions are updated (instead of each node in the regions). This regionization was implemented in previous work for single wavelength optical property reconstructions, and has been extended here for direct spectral recovery. The second approach, using soft-prior information, incorporates prior structure through regularization, which has been discussed in detail elsewhere.[9]

In this work, the spatial prior and spectral constrained methods were combined to produce optimal results. Hard priors were used to incorporate spatial information from MRI. Figure 1(a) is a standard MRI image, which defines the boundary and structural composition of the breast. The mesh in Fig. 1(b) is generated based on the MRI image. Figure 1(c) is the image of the regions constructed from the structural information provided in Fig. 1(a). The black zone is the adipose layer and the white area is fibroglandular tissue. Based on previous simulations and experiments,[33] the hard-priors approach without spectral constraints is sensitive to noise in the measurement data as well as errors in segmentation.

An important issue for spectral constrained reconstruction is the combination of wavelengths, which includes the spectral range of wavelength and sampling of wavelengths in some limited range. A mathematical approach can be used to explore the theoretical choice of the number of useful wavelengths to achieve a certain tolerance in spectroscopy,

and tools such as singular value decomposition (SVD) have been used in previous studies. However, in practice this choice of a certain number of wavelengths depends on the complexity of the field to be recovered and the contrast and chromorphores, so there is actually no useful single cut off point in the number of wavelengths. Rather than take this theoretical approach, here a practical focus was applied, and the spectral range available (310 nm) was divided by the spectral bandwidth of the laser (10 nm), to indicate that a maximum of 31 wavelengths was possible experimentally. In this work, the whole chromophore spectrum was considered equally important with consideration of experimental capability. Therefore, simulated datasets of 6 and 31 wavelengths were compared to study the advantage of introducing more spectral constraints. Six wavelengths were chosen based on our existing NIR system (650, 750, 800, 820, 840, and 850 nm); 31 wavelengths were chosen uniformly between 650 and 950 nm with a 10-nm interval. Random Gaussian-distributed noise was imposed and assumed to be 1% in amplitude and 1 deg in phase. In addition to FD data, cw simulations were added to the FD case of sparse (six) wavelengths by using the FD results as an initial estimate. A cw case with 31 wavelengths was compared with the frequency domain data to evaluate the importance of phase shift.

2.2 Experiments

In this work, a mode-locked Ti:sapphire laser tunable in wavelength from 690 to 1020 nm was used as the light source instead of fixed wavelength diode lasers. The pulsed light occurs at the mode lock frequency of 80 MHz, and is detected with photomultiplier tubes (PMTs). The intrinsic electric signals from the Ti:sapphire laser, synchronized with the light transmissions, were used to heterodyne down the PMT response to low frequency (~1 kHz). Although this mode-lock frequency varies around 80 MHz, it is tracked by taking the Fourier transform of the heterodyned signal and detecting the maximum value. Additionally, the mode-lock frequencies vary with wavelength change, but the effect is precalibrated in software. The low frequency heterodyned-detected signals are put through bandpass filters and amplified 100×, and then read through a multichannel analog-to-digital data acquisition board. The power of the light signal applied to tissue is about 30 mW at the center wavelength of 800 nm, with the available power reaching 2.9 W at the laser output. The geometry of source fiber and detectors has been presented in our previous work.[34] The detail about phase-lock detection using Ti:sapphire laser is discussed somewhere else.[35] Greater power levels can be used in thicker tissues, although adherence to the medical safety limit of 1 W/cm^2 is critical as well. Phantom experiments were carried out using measurement wavelengths from 690 to 850 nm.

A phantom composed of porcine gelatin (Fisher Scientific), TiO_2 powder (Fisher Scientific), porcine blood, and saline was made with heterogeneous targets for hemoglobin measurement. The gelatin was heated to 40°C Celsius for a time of 1 min in a microwave oven. Precalculated quantities of blood were added into the mixture during the stirring and cooling process. Stirring of the TiO_2 powder into the heated gelatin was done for 40 minutes with an automated stir bar, and after the solution was cooled to below 30°C, the blood was added. The total hemoglobin (Hbt) in the background of the gelatin phantom was 15 μM. After refrigeration for 1 h, the gelatin phantom was ready for imaging and holes were filled with blood solutions of 30-μM Hbt and 1% Intralipid. The radius of phantom is 44 mm, and two holes with radius 18 and 20 mm are located in the middle, as shown in Fig. 6(a). The scattering properties were expected to be homogeneous, based on the fact that the Intralipid could be matched to the scattering of the background as determined in a previous phantom study.[33]

3 Results

3.1 Effect of Spatial Prior Information in Different Geometries

The parameters used in this simulation example are listed in Table 1. The targets of chromophores were located at different positions to study the dependence on each other, so that cross talk among different targets can be shown in simulation results. Scattering properties were assumed homogeneous in this part of simulation to simplify this problem with chromophore contrast at different positions. Simulation with scattering contrast is discussed later. Figure 2(a) shows the direct spectral reconstruction with a circular mesh, which was analyzed using three different types of data. Although artifacts and blurring of the boundary can be seen, the FD case using 31 wavelengths yields less noise in the background as compared to the other two cases. Increasing the wavelength bandwidth improves the water image significantly, as shown in both the cw and FD 31 wavelength cases. This results because the main feature in the spectrum of water occurs above 850 nm, so longer wavelengths increase the weight of water relative to HbO_2 and Hb in the reconstruction.[36] Figure 2(b) shows the same example with spatial information incorporated into the reconstruction using hard priors. The recovery error in the three chromophore targets and the dependence of the water image on HbO_2 contrast appear in bar graphs in Fig. 2(c). As indicated in Figs. 2(b) and 2(c), the cw and FD results with 31 wavelengths show significant improvement in the recovery of HbO_2 and water, and a decrease in the dependence between them. Using multiple wavelengths has been suggested as one way to solve the nonuniqueness of the inverse problem when using cw data.[37] As shown here, chromophores have little cross talk into scattering amplitude, while they have significant cross talk in scattering power, even with spatial information and spectral constraints. This occurs because scattering power is more sensitive to noise as compared to other parameters.[38] The ability to uniquely resolve scatter power from continuous wave data alone appears poor at this point, but further study of this issue is needed to make clear conclusions, and the result will likely depend on the complexity of the scatter power variations in the imaging field.

A breast mesh with layered structure and complex boundaries [Fig. 1(b)] was generated from MRI images to simulate realistic clinical situations. The simulation parameters for this example are listed in Table 2. Figures 3(a) and 3(b) are the spectral reconstruction results without and with prior spatial information, respectively. Compared with the simple geometry, the contrast of targets was chosen to be the same as Fig. 2. The results in Fig. 3(a) are not as good as the circular case in Fig. 2(a) because of the complex boundary and internal structure of a realistic breast. It is difficult to identify the targets in the six wavelength FD case. The cw image with 31 wavelengths smoothes the water image results but does not improve the chromophore recovery, while the FD case with 31 wavelengths shows better localization and smoother images of the chromophores. Thus, the results in Fig. 3(a) indicate that for complex geometries, frequency domain data with more wavelengths is important for better reconstruction. Reconstruction is shown to be improved significantly in Figs. 3(b) and 3(c) from the incorporation of prior spatial knowledge. Similar to the simple circular geometry, the FD data from 31 wavelengths produce the best images in terms of quantification of targets and increasing the independence of the individual chromophore estimates.

3.2 Impact of False Prior Information

In clinical studies, perfect structural information may be unlikely because of the low specificity of breast MRI, or even worse, areas that are falsely identified as tumor regions could occur. To complete a preliminary analysis of how this phenomenon might impact the images, some false positive abnormities were created that may not have NIR features. In this

case, those regions will be falsely assumed to exist as prior spatial information in the NIR reconstruction, which may cause errors in the estimation of chromophore and scattering parameters. Figure 4(a) simulates a false positive cyst as a region with a high concentration of water but no hemoglobin, and a tumor region with contrast at all chromophores and scattering properties. The simulation parameters are listed in Table 3. The cyst presents contrast in the MRI image, making it a common false positive in NIR spectroscopy. The recovery error in water, cyst, and the dependence on HbO_2 is shown in Fig. 4(b). The FD case involving 31 wavelengths again leads to the least amount of cross talk and the most accurate estimation of the concentration of water and cyst.

3.3 Experimental Studies

The simulation examples show that incorporating more spectral constraints with spatial priors should optimize NIR spectroscopy in terms of improving the accuracy of the estimation of the concentration of chromophores and decreasing the dependence between them. The effects of introducing a false positive region are also evident, albeit limited in impact when many wavelengths are used. These results can be used to guide the design of the hardware setup of an imaging system. Using a Ti:sapphire laser, multiwavelength frequency domain measurements can be acquired over the range of 690 to 840 nm through PMT detection. The phantom used in this study is shown in Fig. 5. Total hemoglobin (Hbt) in the background of the gelatin phantom was 15 μM. Blood with 30 μM of Hbt and 1% intralipid was put in the holes to create an imaging target, as shown in Fig. 5(a). Figure 6 shows the simulation results based on this gelatin phantom design. The position of two targets was chosen based on the gelatin phantom shown in Fig. 5(a). Since the information about blood in the experiment is total hemoglobin, the contrast of targets and background are displayed with the same total hemoglobin concentration as in the experiment. The Gaussian-distributed noise was assumed to be 2% in amplitude and 1% in phase. Three different wavelength sets were used for spectral reconstruction, based on the sampling wavelengths in experiment. Experimental spectral reconstruction results using the same three sets of wavelengths are shown in Fig. 6(b) and a cross sectional profile of Hbt is presented in Fig. 6(c). Although any wavelength between 690 to 850 nm can be chosen for detection, the final sampling wavelengths were limited by issues inherent in the present experimental setup. Only those wavelengths at a stable lock-in detection frequency condition could be used for measurement, and the Ti:sapphire laser does have specific wavelengths where the frequency lock is less stable than others. The experimental details will be discussed in another more detailed instrumentation study, yet even so, at least twice the number of wavelengths in the PMT detection range can be taken in this Ti:sapphire-based system compared to our existing diode laser system. As shown in Fig. 6(b), the two targets are hardly evident in the four and six wavelength cases without spatial information, whereas the reconstruction from 12 wavelengths of data estimates the locations of the two targets of Hbt very clearly. The results from the 12 wavelength case also show smoother images of the other chromophores and scattering parameters. The cross sectional profile indicates that the recovered Hbt concentrations are inaccurate in the four and six wavelength cases, while the values from the case with 12 wavelengths of data are much closer to the true results. The experimental total-hemoglobin result with 12 wavelengths is quite consistent with the simulation in Fig. 5. Since the impact of systematic error is usually hard to predict in the realistic experimental process, the comparison between experiment and simulation is fair. The simulation indicates that promising results are possible with low noise dependence in the case of more wavelengths. Figures 6(d) and 6(e) show spectral reconstruction with prior region information. Here, the Hbt images from four and six wavelengths of data were improved significantly compared to Fig. 6(b). The cross sectional results again show that 12 wavelengths of data produce a better target contrast due to the improvement in the recovery of background values.

4 Discussion

The analysis of imaging with diffuse light shown in Figs. 2 and 3 illustrates the possible improvements with 1. added wavelengths, 2. frequency domain versus continuous wave data, and 3. spatial prior information. While most of the images in Fig. 2 appear comparable, accuracy in the water and scattering images is more difficult to achieve. Quantification improves as more wavelengths are used, and as FD data are made available; however, errors near 13% in water quantification and well over 25% in scatter power remain. Simulations performed on the more realistic breast geometry in Fig. 3 produce similar results, except that the background noise is considerably higher. Again, adding more wavelengths and using FD versus cw data generally improves all images. The addition of spatial priors improves the accuracy of recovery of the parameters in the predefined regions. The error in water concentration is about 15% for FD data with six wavelengths; this decreases to less than 10% as more wavelengths of cw data are used, and it is reduced to 1% when FD data with many wavelengths is introduced. Similar trends were observed in the error behavior associated with the dependence of the water image on HbO_2 contrast, which was decreased from about 12 to 3%. Errors introduced by false positive regions identified in MRI are an important consideration for MRI-guided NIR spectroscopy. The technique must be sufficiently accurate in the face of these regions to estimate their true properties. The results shown in Fig. 4 indicate again that many wavelengths and frequency domain data would always be superior.

In the experimental validation of the simulation findings, the improvement with more wavelengths is apparent, as is the improvement with spatial prior information. The values of water for different cases are consistent between the diffuse reconstruction and the spatial prior reconstruction. The scattering power of the spatial reconstruction has very low values with high region errors, especially with four and six wavelengths, which are related to the high sensitivity to noise and potential error introduced in region estimation. Unfortunately, in the case of reconstruction with spatial priors, the scatter power is still in error well over 30%, making it unclear how accurately this parameter can ultimately be recovered. Another difficulty in validating scattering properties is the limitation of our ability to accurately quantify them in controlled experiments. As in the gelatin phantom experiment, the scatters in the background is TiO_2 powder, while scatters in the target solution are Intralipid. The simulation results in Fig. 4 shows smooth image of scattering amplitude, and scattering power shows relatively higher error, as in other examples.

The question of wavelength selection has been investigated in the cases of frequency domain and continuous wave data.[36,37] The essence of spectral reconstruction was to quantify different chromophores as independently as possible with sufficient spectral information. The simulation and experimental results are consistent with the findings from previously published work, and indicate that an increased number of wavelengths within a fixed range would be superior. Expansion of this wavelength range to longer values, albeit with only cw light transmission, is under investigation and may lead to further improvements. However, for now, it has been shown that a frequency domain measurement with up to 12 wavelengths is possible, and provides a superior dataset for image-guided spectroscopy of tissue, as compared to the existing six wavelength approach, or to a cw approach limited to 650–850-nm range. As mentioned previously the combination of additional wavelengths will be further explored both theoretically and experimentally, when the experimental system to test this has been completed.

5 Conclusions

In conclusion, simulations with different geometries and experimental gelatin phantom studies show the need to improve NIR spectroscopy by maximizing broadband wavelength information used in spectral-based recovery, even when using prior spatial information from other clinical modalities. The accuracy of the chromophore estimates can be improved and the potential false positive regions can be better eliminated when using spectral reconstruction with maximal spectral content. The experimental data also indicate that there is a potential advantage of spectral reconstruction in limiting the background variation in otherwise homogeneous regions of tissue. The simulations provide important guidance for system development. A new Ti:sapphire-based system has been developed to validate the need for inclusion of many wavelengths of frequency domain data not previously possible due to a limited range of wavelengths that can be obtained commercially with diode lasers. The next step is to extend the spectral range to higher wavelengths, possibly with a combination of cw and FD detection, which should improve the water estimation accuracy.

Acknowledgments

This work has been funded by National Cancer Institute research grants PO1CA80139, U54CA105480, and K25 CA106863.

References

1. Hata T, Takahashi H, Watanabe K, Takahashi M, Taguchi K, Itoh T, Todo S. Magnetic Resonance Imaging for Preoperative Evaluation of Breast Cancer: A Comparative Study with Mammography and Ultrasonography. J Am Coll Surg. 2004; 198:190–197. [PubMed: 14759774]
2. Ntziachristos V, Yodh AG, Schnall M, Chance B. Concurrent MRI and diffuse optical tomography of breast after indocyanine green enhancement. Proc Nat Acad Sci USA. 2000; 97:2767–2772. [PubMed: 10706610]
3. Carpenter CM, Pogue BW, Jiang S, Dehghani H, Wang X, Paulsen KD, Wells WA, Forero J, Kogel C, Weaver JB, Poplack SP, Kaufman PA. Image-guided optical spectroscopy provides molecular-specific information in vivo: MRI-guided spectroscopy of breast cancer hemoglobin, water and scatterer size. Opt Lett. 2007; 32:933–935. [PubMed: 17375158]
4. Brooksby B, Pogue BW, Jiang S, Dehghani H, Srinivasan S, Kogel C, Tosteson T, Weaver JB, Poplack SP, Paulsen KD. Imaging breast adipose and fibroglandular tissue molecular signatures using hybrid MRI-guided near-infrared spectral tomography. Proc Nat Acad Sci USA. 2006; 103:8828. [PubMed: 16731633]
5. Barbour RL, Graber HL, Chang J, Barbour SS, Koo PC, Aronson R. MRI-guided optical tomography: prospects and computation for a new imaging method. IEEE Comput Sci Eng. 1995; 2:63–77.
6. Arridge SR, Schweiger M. Sensitivity to prior knowledge in optical tomographic resconstruction. Proc SPIE. 1995; 2389:378–388.
7. Pogue BW, Paulsen KD. High resolution near infrared tomographic imaging simulations of rat cranium using apriori MRI structural information. Opt Lett. 1998; 23:1716–1718. [PubMed: 18091894]
8. Ntziachristos V, Hielscher AH, Yodh AG, Chance B. Diffuse optical tomography of highly heterogeneous media. IEEE Trans Med Imaging. 2001; 20:470–478. [PubMed: 11437107]
9. Brooksby B, Jiang S, Dehghani H, Pogue BW, Paulsen KD, Weaver JB, Kogel C, Poplack SP. Combining near infrared tomography and magnetic resonance imaging to study in vivo breast tissue: implementation of a Laplacian-type regularization to incorporate MR structure. J Biomed Opt. 2005; 10:050504.
10. Yalavarthy PK, Pogue BW, Dehghani H, Paulsen KD. Weight-matrix structured regularization provides optimal generalized least-squares estimate in diffuse optical tomography. Med Phys. 2007; 34:2085–2098. [PubMed: 17654912]

11. Durduran T, Choe R, Culver JP, Zubkov L, Holboke MJ, Giammarco J, Chance B, Yodh AG. Bulk optical properties of healthy female breast tissue. Phys Med Biol. 2002; 47:2847–2861. [PubMed: 12222850]
12. Pogue BW, Paulsen KD, O'Hara JA, Swartz HM. Estimation of oxygen distribution in RIF-1 tumors by diffusion model-based interpretation of pimonidazole-hypoxia and Eppendorf measurements. Rad Res. 2001; 155:15–25.
13. Tromberg BJ, Shah N, Lanning R, Cerussi A, Espinoza J, Pham T, Svaasand L, Butler J. Non-invasive in vivo characterization of breast tumors using photon migration spectroscopy. Neoplasia. 2000; 2:26–40. [PubMed: 10933066]
14. Ntziachristos V, Kohl M, Ma H, Chance B. Oximetry based on diffuse photon density wave differentials. Med Phys. 2000; 27:410–421. [PubMed: 10718146]
15. Cubeddu R, D'Andrea C, Pifferi A, Taroni P, Torricelli A, Valentini G. Effects of the menstrual cycle on the red and near-infrared optical properties of the human breast. Photochem Photobiol. 2000; 72:383–391. [PubMed: 10989610]
16. Zhu Q, Kurtzma SH, Hegde P, Tannenbaum S, Kane M, Huang M, Chen NG, Jagjivan B, Zarfos K. Utilizing optical tomography with ultrasound localization to image heterogeneous hemoglobin distribution in large breast cancers. Neoplasia. 2005; 7:263–270. [PubMed: 15799826]
17. Chance B, Nioka S, Zhang J, Conant EF, Hwang E, Briest S, Orel SG, SMD, Czerniecki BJ. Breast cancer detection based on incremental biochemical and physiological properties of breast cancers: a six-year two-site study. Acad Radiol. 2005; 12:925–933. [PubMed: 16023383]
18. Intes X, Maloux C, Guven M, Yazici T, Chance B. Diffuse optical tomography with physiological and spatial *a priori* constraints. Phys Med Biol. 2004; 49:N155–N163. [PubMed: 15272687]
19. Srinivasan S, Pogue BW, Brooksby B, Jiang S, Dehghani H, Kogel C, Wells WA, Poplack S, Paulsen KD. Near-infrared characterization of breast tumors in-vivo using spectrally-constrained reconstruction. Technol Cancer Res Treat. 2005; 4:513–526. [PubMed: 16173822]
20. Pogue BW, Jiang S, Dehghani H, Kogel C, Soho S, Srinivasan S, Song X, Tosteson TD, Poplack SP, Paulsen KD. Characterization of hemoglobin, water, and NIR scattering in breast tissue: analysis of intersubject variability and menstrual cycle changes. J Biomed Opt. 2004; 9(3):541–552. [PubMed: 15189092]
21. Arridge SR, Lionheart WRB. Nonuniqueness in diffusion-based optical tomography. Opt Lett. 1998; 23:882–884. [PubMed: 18087373]
22. Schweiger M, Arridge SR. Direct calculation with a finite-element method of the Laplace transform of the distribution of photon time of flight in tissue. Appl Opt. 1997; 36:9042–9049. [PubMed: 18264463]
23. Patterson, MS.; Madsen, SJ.; Moulton, JD.; Wilson, BC. Microwave Theory and Techniques Symposium Digest. IEEE; New York: 1991. Diffusion equation representation of photon migration in tissue; p. 905-908.
24. Paulsen KD, Jiang H. Spatially varying optical property reconstruction using a finite element diffusion equation approximation. Med Phys. 1995; 22:691–701. [PubMed: 7565358]
25. Jiang H, Paulsen KD, Osterberg UL, Pogue BW, Patterson MS. Optical image reconstruction using frequency-domain data: simulations and experiments. J Opt Soc Am A. 1996; 13:253–266.
26. Schweiger M, Arridge SR. The finite-element method for the propagation of light in scattering media: frequency domain case. Med Phys. 1997; 24:895–902. [PubMed: 9198025]
27. Patterson MS, Wilson BC, Wyman DR. The propagation of optical radiation in tissue I. models of radiation transport and their application. Lasers Med Sci. 1990; 6:155–168.
28. McBride TO, Pogue BW, Gerety E, Poplack S, Osterberg UL, Paulsen KD. Spectroscopic diffuse optical tomography for quantitatively assessing hemoglobin concentration and oxygenation in tissue. Appl Opt. 1999; 38:5480–5490. [PubMed: 18324057]
29. van Staveren HJ, Moes CJM, van Marle J, Prahl SA, van Gemert MJC. Light scattering in Intralipid-10% in the wavelength range of 400–1100nm. Appl Opt. 1991; 30:4507–4514. [PubMed: 20717241]
30. Mourant JR, Fuselier T, Boyer J, Johnson TM, Bigio IJ. Predictions and measurements of scattering and absorption over broad wavelength ranges in tissue phantoms. Appl Opt. 1997; 36:949. [PubMed: 18250760]

31. Brooksby B, Dehghani H, Pogue BW, Paulsen KD. Near infrared (NIR) tomography breast image reconstruction with a priori structural information from MRI: algorithm development for reconstructing heterogeneities. IEEE J STQE. 2003; 9:199–209.

32. Dehghani H, Pogue BW, Jiang S, Brooksby B, Paulsen KD. Three dimensional optical tomography: resolution in small object imaging. Appl Opt. 2003; 42:135–145. [PubMed: 12518832]

33. Brooksby, B. Engineering. Dartmouth College; Hanover, NH: 2005. Combined near-infrared tomography and MRI to improve breast tissue chromophore and scattering assessment; p. 228

34. McBride TO, Pogue BW, Jiang S, Osterberg UL, Paulsen KD. A parallel-detection frequency-domain near-infrared tomography system for hemoglobin imaging of the breast *in vivo*. Rev Sci Instrum. 2001; 72:1817–1824.

35. Wang, J.; Jiang, S.; Pogue, BW.; Paulsen, KD. Enhanced NIR spectral reconstruction with Ti:sapphire laser based frequency-domain system. Proceedings of the OSA Biomed. Topical Meetings; 16–19 March 2008; St Petersburg, FL.

36. Cerussi AE, Jakubowski D, Shah N, Bevilacqua F, Lanning R, Berger AJ, Hsiang D, Butler J, Holcombe RF, Tromberg BJ. Spectroscopy enhances the information content of optical mammography. J Biomed Opt. 2002; 7(1):60–71. [PubMed: 11818013]

37. Corlu A, Durduran T, Choe R, Schweiger M, Hillman EM, Arridge SR, Yodh AG. Uniqueness and wavelength optimization in continuous-wave multispectral diffuse optical tomography. Appl Opt. 2003; 28:2339–2341.

38. Wang J, Davis SC, Jiang S, Pogue BW, Paulsen KD. Convergence analysis and preliminary experimental feasibility for MRI-localized region spectroscopy with NIR diffuse optical tomography. Proc SPIE. 2007; 6434:64341B.

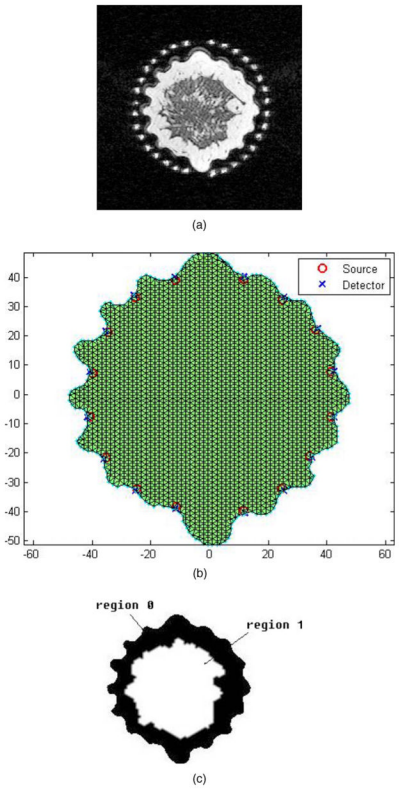

Fig. 1.
(a) MRI image of breast. (b) Mesh for NIR reconstruction generated from MRI image. (c) Region segmentation based on MRI image.

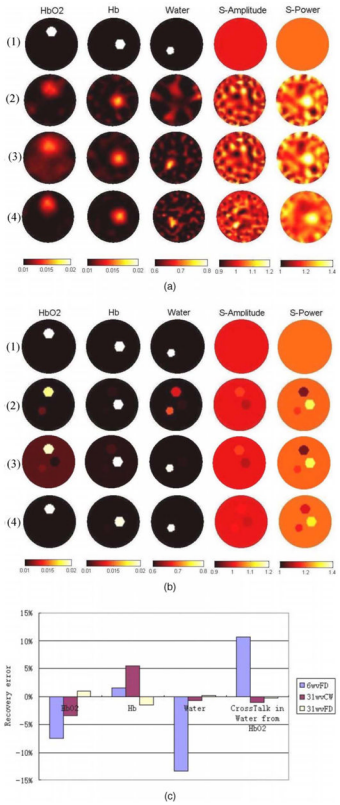

Fig. 2.

(a) Direct spectral reconstruction images of a circular geometry. The top row (1) shows the true values of the background and targets. The second, third, and fourth rows present reconstruction results based on: (2) frequency domain (FD) data from six wavelengths, (3) cw data from 31 wavelengths, and (4) FD data from 31 wavelengths. (b) Direct spectral reconstruction images using hard priors. Perfect segmentation is assumed in terms of region size and location. Top row (1) shows the true values as in (a) The lower three rows show the hard prior reconstructions with: (2) FD data from six wavelengths, (3) cw data from 31 wavelengths, and (4) FD data from 31 wavelengths. (c) Errors in recovered properties of HbO_2, Hb, water, and cross talk in the water image from HbO_2 contrast using hard priors. The cross talk is defined as the error in the recovered value of water, at the position of HbO_2 contrast.

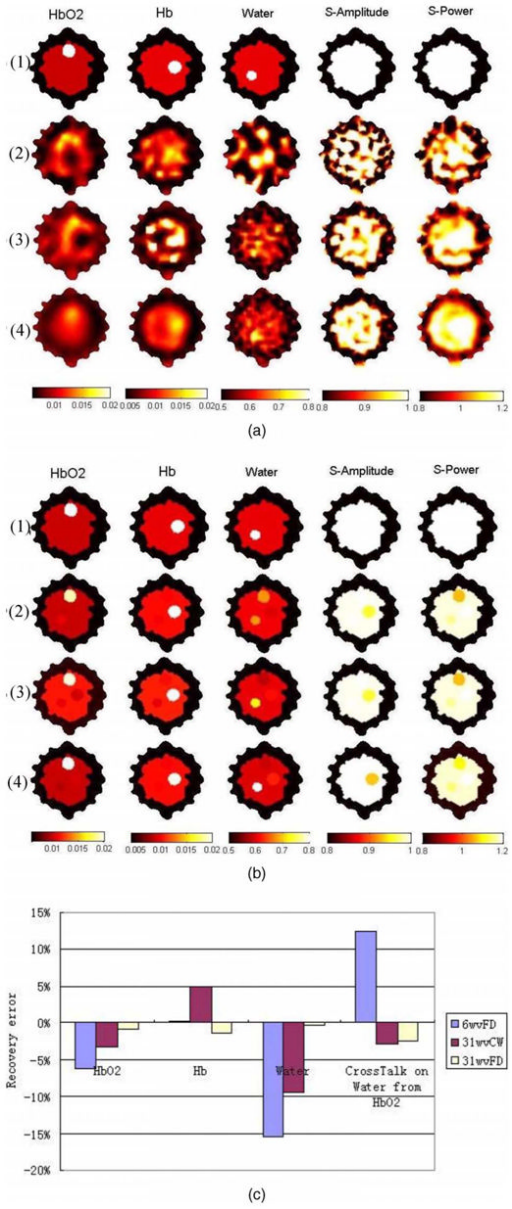

Fig. 3.

(a) Direct spectral reconstruction images of a two-layer (adipose and glandular tissue) MRI-based geometry. The top row (1) shows the true values of background and targets. The lower three rows show reconstruction results based on: (2) FD data from six wavelengths, (3) cw data from 31 wavelengths, and (4) FD data from 31 wavelengths. (b) Spectral reconstruction images of the two-layer breast geometry with hard priors. Exact region segmentation is assumed. The top row (1) shows the true values of background and targets. The lower three rows show reconstruction results based on: (2) FD data from six wavelengths, (3) cw data from 31 wavelengths, and (4) FD data from 31 wavelengths. (c) Errors in recovered properties of HbO_2, Hb, water, and cross talk in water image from HbO_2 contrast in (b).

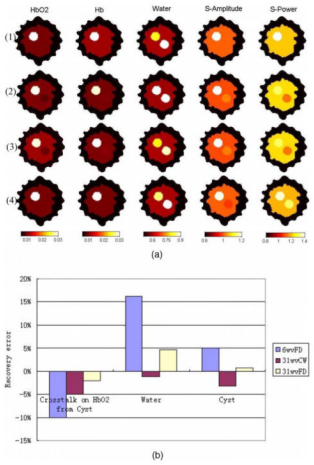

Fig. 4.

(a) Spectral reconstruction images with a simulated false positive cyst. Top row (1) shows the true values of background and three targets of chromophores and cyst. Lower rows show reconstruction results based on: (2) FD data from six wavelengths, (3) cw data from 31 wavelengths, and (4) FD data from 31 wavelengths. (b) Recovered error in water and cyst values and cross talk in the HbO_2 image from the simulated cyst region.

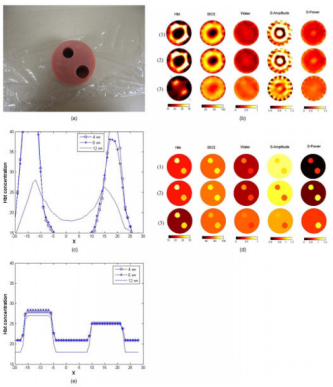

Fig. 5.

(a) Gelatin phantom (r=44 mm) with two holes of radii 18 and 20 mm, respectively. Direct spectral reconstruction images with different numbers of wavelengths are shown in (b), where row (1) involves four wavelengths (695, 750, 800, and 830 nm), row (2) involves six wavelengths (695, 710, 750, 780, 800, and 830 nm), and row (3) involves 12 wavelengths (695, 700, 710, 725, 735, 750, 770, 780, 800, 810, 820, and 830 nm). Cross sectional values of Hbt [along the line shown in (b)] are shown in (c) for all three wavelength sets. (d) Spectral reconstruction images using hard-prior region information from datasets with 4, 6, and 12 wavelengths, respectively. (e) Cross section of Hbt in the images in (d) for all three wavelength sets.

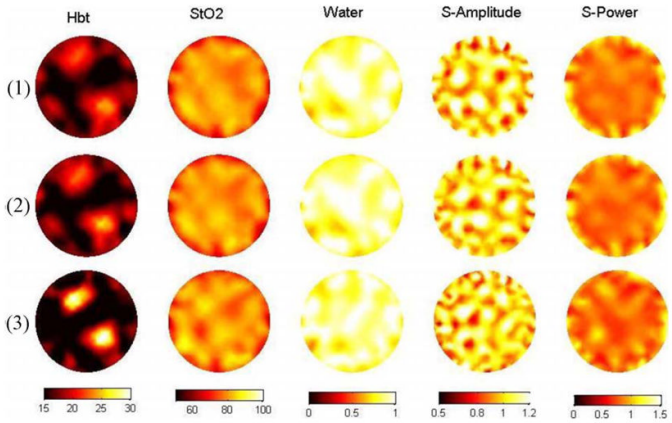

Fig. 6.

Simulation of two-target phantom with known contrast in total hemoglobin (Hbt). Row (1) involves four wavelengths (695, 750, 800, and 830 nm), row (2) involves six wavelengths (695, 710, 750, 780, 800, and 830 nm), and row (3) involves 12 wavelengths (695, 700,710, 725, 735, 750, 770, 780, 800, 810, 820, and 830 nm). These choices match the experimental study shown in Fig. 6.

Table 1

Parameters of simulation example in Fig. 2.

	HbO_2 (mM)	Hb (mM)	Water (%)
Background	0.01	0.01	0.6
Target	0.02	0.02	0.8

Table 2

Parameters of simulation example in Fig. 3.

	HbO_2 (mM)	Hb (mM)	Water (%)
Adipose	0.006	0.004	0.5
Glandular	0.01	0.01	0.6
Target	0.02	0.02	0.8

Table 3

Parameters of simulation example in Fig. 4.

	HbO_2 (mM)	Hb(mM)	Water (%)	S-Amp. [10^{-3b}(mm)$^{b-1}$]	S-power	Cyst (%)
Adipose	0.006	0.004	0.5	0.8	0.8	—
Glandular	0.01	0.01	0.6	1	1.2	—
Target	0.03	0.03	0.8	1.2	1.4	0.9